2.5D Particle and MHD simulations of mini-magnetospheres at the Moon

Erika M. Harnett and Robert M. Winglee

Department of Earth and Space Sciences, University of Washington, Seattle, Washington, USA

Received 2 January 2002; revised 22 May 2002; accepted 4 June 2002; published 4 December2002.

[1] 2.5D Particle simulations of the solar wind interaction with the magnetized regions on the surface of the Moon confirm the earlier 2D MHD result that mini-magnetospheres can form around the magnetic anomalies. A dipole buried 100 km below the surface with a field strength equal to 50 nT at the surface and 10 nT at 100 km above the surface held the solar wind off of the surface and caused a bow shock and a magnetopause to form. However, the boundary separating the bow shock and magnetopause becomes ambiguous as the two structures merge due to the small-scale size of the mini-magnetospheres. Acceleration of solar wind particles occurs at the shock. Inside the magnetopause, the Lunar electrons remained highly magnetized and exhibited fluid-like behavior. The Lunar ions, on the other hand, become demagnetized. Outside of the magnetopause, the solar wind ions and electrons exhibited fluid-like behavior. Small-scale and nonideal MHD effects can be included into fluid simulations by adding Hall and pressure gradient terms in Ohm's Law, creating a magnetoplasma dynamics (MPD) model. The small-scale effects allow for field-aligned currents and electric fields that look qualitatively similar to those in the particle simulations, but they do not appear to change the overall shape of the mini-magnetosphere. The extra components of the electric field indicate the presence of charge separation at the shock surface, due to the momentum difference between ions and electrons, and the near the Lunar surface, due to nonideal MHD behavior inside the mini-magnetosphere. The 2.5D MPD model can replicate the ion demagnetization seen in the 2.5D particle simulations. *INDEX TERMS:* 2753 Magnetospheric Physics: Numerical modeling; 1517 Geomagnetism and Paleomagnetism: Magnetic anomaly modeling; 2756 Magnetospheric Physics: Planetary magnetospheres (5443, 5737, 6030); 6250 Planetology: Solar System Objects: Moon (1221)

Citation: Harnett, E. M., and R. M. Winglee, 2.5D Particle and MHD simulations of mini-magnetospheres at the Moon, *J. Geophys. Res.*, *107*(A12), 1421, doi:10.1029/2002JA009241, 2002.

1. Introduction

[2] While orbiting above regions of large crustal magnetization facing into the solar wind, Lunar Prospector encountered structures at the Moon that had the particle and magnetic field signatures similar to a bow shock and magnetopause [*Lin et al.*, 1998]. One signature was the appearance, disappearance and then reappearance of a modification of the electron flux and an increase in magnetic field strength at 100 km that seemed to fluctuate with solar wind conditions. Further analysis of the particle data indicated that the energy spectrum of the electrons changed as the satellite traversed a bow shock-like structure and that plasma waves were present outside of this shock-like region. They concluded that Lunar Prospector had encountered a mini-magnetosphere.

[3] The measurement of strong surface magnetic fields at the Moon is not new. Magnetometer measurements over portions of the Moon by the Apollo satellites provided the first evidence for magnetic anomalies on the surface [*Sharp*, 1973; *Dyal*, 1974; *Hood et al.*, 1981] (with a summary in the work of *Lin et al.* [1988]). Apollo measurements suggested surface field strengths on the order of 100 nT and small regions greater than 1000 nT [*Dyal*, 1974], with the magnitude on the order of 2 nT at 100 km above the surface. And shock like structures may have been seen by the Apollo 15 and 16 satellites. *Russell and Lichtenstein* [1975] analyzed "limb compressions" and found that it was highly likely that these amplifications of the IMF were due to deflection of the solar wind by the anomalies while the size of the compression was controlled by the direction of the IMF.

[4] *Hood and Williams* [1989] estimated the deflection of the solar ions wind by small anomalous regions (100–200 km in diameter) with surface field strengths greater than 1000 nT by following the trajectories of single particles. They then combined the results from an array of single particle trajectories to estimate how much the surface flux would be reduced by the presence of the magnetic anomalies. They modeled the anomalous regions with 9–15 buried dipoles that produced a total magnetic field strength of approximately 2 nT at 100 km above the surface. Hood and Williams found significant deflection of the particles for

0148-0227/02/2002JA009241$09.00

surface field strengths greater than 1000 nT and almost no deflection for surface field strengths less than 800 nT. Their approach had the advantage that it was 3D. The disadvantage to their approach though was that it could not take collective effects into account and therefore was not a self-consistent, particle simulation. It could not predict the presence of shocks, heating or modification of the surface magnetic field.

[5] 2D MHD simulations of the solar wind interaction with the Lunar magnetic anomalies [*Harnett and Winglee*, 2000] agreed with the analysis that LP encountered a ''mini-magnetosphere'' (a small-scale magnetosphere) over the magnetic anomaly in the Serenitatis antipode. A mini-magnetosphere would form in the MHD simulations when the field strength of the magnetic anomaly was 290 nT at the surface and greater than 10 nT at 100 km above the surface, for solar wind velocity and density equal to 400 km/s and $10/cm^3$, respectively. The results also indicated that mini-magnetospheres are much more dynamic than planetary sized magnetospheres. Simply flipping the direction of the IMF caused the mini-magnetosphere to inflate and completely change shape. The distance between the outer shock surface and the surface increased from 100 km to 190 km, and the shock surface went from elongated along the Lunar surface to round with a smaller lateral extent. One limitation of the model was that the strength of the magnetic field at 100 km above the surface needed to be an order of magnitude larger than observed values in order for mini-magnetospheres to form at satellite altitudes.

[6] The largest mini-magnetospheres that formed in the MHD simulations, with a scale size near 200 km, contained internal structures larger than a proton gyroradius. But the smallest mini-magnetospheres had a scale size smaller than 100 km and the size of the proton gyroradius became comparable to the size of the internal structure. This suggests that the smallest mini-magnetospheres in the simulations approached the limit where ideal MHD breaks down and particle simulations should be employed to help predict the behavior of the plasma inside the bow shock. It also indicates the need for an extended MHD model that incorporate small-scale and nonideal MHD effects into the fluid model.

[7] To fully simulate the particle behavior near the magnetic anomalies, a multiparticle simulation must be done. Self-consistent particle simulations predict the paths of many particles as they interact with each other and the electric and magnetic fields. The particle interactions can also modify existing magnetic and electric fields, as charge and current densities evolve. The resolution of particle simulations though tends to be coarser than for fluid simulations due to the computationally intensive nature of the simulations and the smoothing needed to reduce noise.

[8] MHD simulations can be extended to incorporate small-scale dynamics like that seen in particle simulations. *Winglee* [1994] showed that including a Hall term and a pressure gradient term in the Ohm's Law equation for the electric field reproduced surface plasma currents seen in particle simulations but not in ideal MHD simulations. The deviations from the ideal MHD regime in particle simulations could be accounted for by the Hall term. The localized charge separation that can also occur in particle simulations could be incorporated into MHD through a pressure gradient in Ohm's Law. This magnetoplasma dynamics (MPD) model includes electric fields generated by charge separation and accounts for deviations from ideal MHD, while remaining a fluid model. 2.5D simulations have the advantage over 2D simulations in that all three dimensions of the momentum, current and electric and magnetic field quantities are present. But the 2.5D simulations are limited to 2 spatial dimensions. Thus plasma can only flow around the poles of the obstacle.

[9] In addition to providing insight into magnetospheric dynamics, mini-magnetospheres form in the region where plasma begins to transition from acting collectively as an MHD fluid to one where gyroradius and charge separation effects control the dynamics. Comparison of MPD simulations and particle simulations with data in this regime may help determine how the transition between particle and fluid behavior occurs, with results applicable in a wide range of plasma physics. Magnetic anomalies have also been found on Mars, with the potential for localized magnetic fields existing on other planetary bodies. Identification of other mini-magnetospheres has yet to be made but this work could help determine the signatures to look for.

[10] This paper presents the results from 2.5D particle and MPD simulations of the solar wind interacting with a magnetic anomaly on the surface of the Moon. The 2.5D particle simulations are used to verify that mini-magnetospheres will form around magnetic anomalies, and investigate the particle nature of the resulting mini-magnetospheres. The 2.5D MPD simulations investigate the changes in the characteristic quantities of the mini-magnetospheres when small-scale, nonideal MHD effects are incorporated into the fluid model. The results from both models can then be compared to look for similarities and differences.

2. Particle Simulations

2.1. Model Parameters

[11] The particle simulations used a particle-in-a-cell code [*Winglee and Kellogg*, 1990]. The Lorenz force equation takes the form

$$\frac{\partial \vec{v}}{\partial t} = \frac{q}{m}\left(\vec{E} + \vec{v} \times \vec{B}\right) \tag{1}$$

$$\frac{\partial \vec{r}}{\partial t} = \vec{v} \tag{2}$$

where $\vec{v}$ and $\vec{r}$ are the velocity and position of an individual particle, q and m are the particle charge and mass, and $\vec{E}$ and $\vec{B}$ are the electric and magnetic fields. The particle positions are accumulated on a grid to determine charge density and current density. The charge density is then used to solve Poisson's equation for the electric field. The current density and electric field are then used to solve Maxwell's equations for the magnetic field. All equations are solved in 2D spatially, but in 3D for velocity, magnetic field, electric field and current density. Thus plasma can only flow above and below the Moon, as it acts like an infinite cylinder. A more detailed discussion of the model can be found in the work of *Winglee and Kellogg* [1990].

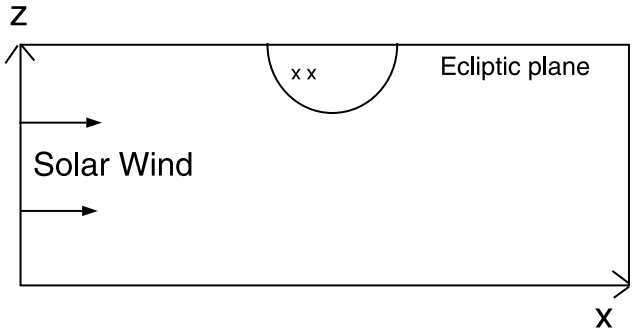

Figure 1. All of the plots for the particle simulations follow this convention. The arrows on the left hand side indicate the direction of the solar wind. Symmetry about the ecliptic plane is assumed. The two small "x"s inside the object indicate the approximate location of the line currents for a dipole field with the moment in the $+\vec{z}$ direction. The vertical axis will be referred to as the $\vec{z}$ axis and the horizontal axis as the $\vec{x}$ axis. The plots for the 2.5D MPD simulations look similar but symmetry about the ecliptic plane is not assumed.

[12] Short scale length electrostatic quantities were solved on a 576 × 288 grid, with longer-wavelength electromagnetic quantities solved on a grid with half the resolution. The resolution of the simulation is such that the solar wind electron Debye length is equal to half a grid unit. The grid space separation was equal to 11.6 km for quantities solved in the finest resolution, but most data was smoothed to remove the effects of noise before analysis, thereby reducing the resolution. The time step throughout the simulation is equal to 1/8 of the electron plasma frequency. The largest frequency considered is on the order of or smaller than the plasma frequency.

[13] The boundary conditions were assumed to be periodic at the top and bottom of the simulation box, with symmetry about the ecliptic plane (Figure 1). In the present case the direction away from the Sun is in the $\vec{x}$ direction and $\vec{z}$ is perpendicular to the ecliptic plane. The velocity in and out of the simulation plane ($\vec{y}$) is initially assumed to be zero. The magnetic field out of the simulations plane ($\vec{B}_y$) is the induced magnetic field created by currents in the simulation plane.

[14] A total of 350,000 multicharged particles were used to represent four distinct particle populations: solar wind ions and electrons, and Lunar ions and electrons. The solar wind was assumed to be composed of an equal number of electrons and H^+ ions, with a solar wind ion to electron mass ratio that was held constant at 64 for all simulations. The solar wind is continuously injected from the left hand side of the box with a number density of 6 particles cm^{-3}. The simulation must be halted before the solar wind reaches the right hand side boundary to prevent reflection effects.

[15] The Lunar ionosphere consisted of an equal number of electrons and ions, where the ion species was varied. The Lunar ion to electron mass ratio was set to 64, 256 or 1024, approximating a surface ion species composed of H^+, Ne^+, or Ar^+ ions, respectively. In order to gain sufficient number statistics at the low Lunar number density, the mass of the Lunar ions and electrons relative to the solar wind mass, not the number density, was decreased. The solar wind electron to Lunar electron mass ratio was held constant at 70 for all simulations, while the solar wind ion to Lunar ion mass ratio varied between 4.4 and 70.

[16] Argon constitutes the largest fraction of ions in the tenuous Lunar atmosphere, with Neon becoming comparable only during periods of extremely high solar flux [*Johnson*, 1971; *Hodges*, 1974]. The average day-side ion density of the Lunar atmosphere is 10^{-1} cm^{-3} and a night-side density 10^{-2} cm^{-3} with a scale height of about 100 kilometers [*Johnson*, 1971; *Hodges*, 1974].

[17] The IMF is set to zero for numerical simplicity. In order to evaluate the influence of the ion gyroradius on forming a mini-magnetosphere, the initial bulk speed of the solar wind was varied between 165 km/s and 1622 km/s, translating to a variation in the gyroradius between 23 km and 255 km. The thermal speed of the solar wind is small compared to the bulk speed and corresponds to a temperature range of 2.22 eV and 220 eV. The Lunar particles were initialized with no bulk speed and a thermal speed equal to a range of temperatures between 0.02 eV and 1.7 eV. The measured temperatures are less than 100 eV for electrons and less than 50 eV for ions in the solar wind [*Parks*, 1991] and 0.04 eV in the Lunar atmosphere [*Johnson*, 1971].

[18] The magnetic anomaly is modeled with a dipole buried approximately 100 km below the surface. The dipole is created using opposing current elements. The current elements are buried at such a large distance from the surface to ensure full grid resolution. To compensate, the magnetic field strength was reduced. The variation of the solar wind ion gyroradius results in a variation of the surface magnetic field strength between approximately 15 nT (for the fastest solar wind bulk speed) and 200 nT (for the slowest solar wind). For the baseline case of the solar wind bulk speed equal to 400 km/s, the magnetic field strength at the Lunar surface is approximately 50 nT and 10 nT at 100 km above the surface. After smoothing the density, the resolution becomes 104.4 km, comparable to the depth of the dipole. But at this time, it is difficult to go to finer resolution.

2.2. Particle Simulation Results

[19] The particle simulations show that the magnetic anomalies can produce significant deflection of the solar wind for anomalous magnetic field measuring 50 nT at the surface and 10 nT at 100 km altitude, when the solar wind had a number density of approximately 6 cm^{-3} and bulk velocity of 400 km/s (Figure 2). The Lunar ion to electron mass ratio is equal to 1024, while the solar wind ion to Lunar ion mass ratio is equal to 4.375. The temperature of the Lunar ions and electrons is 0.02 eV, while the initial temperature of the solar wind ions and electrons is 2.22 eV.

[20] The surface magnetic field is compressed by the solar wind but can still hold the solar wind particles off the surface, creating a boundary that resembles both a bow shock and a magnetopause. The inner edge of this surface forms 160 km above the surface (when measured radially from the surface) (Figures 2a and 2b), and forms a boundary that the solar wind does not cross. This boundary can be clearly seen as a bubble-like feature in the density plots for the solar wind ion and electron populations, Since there is a region where no solar wind particles cross into, the location of the magnetopause is not as ambiguous as in the MHD

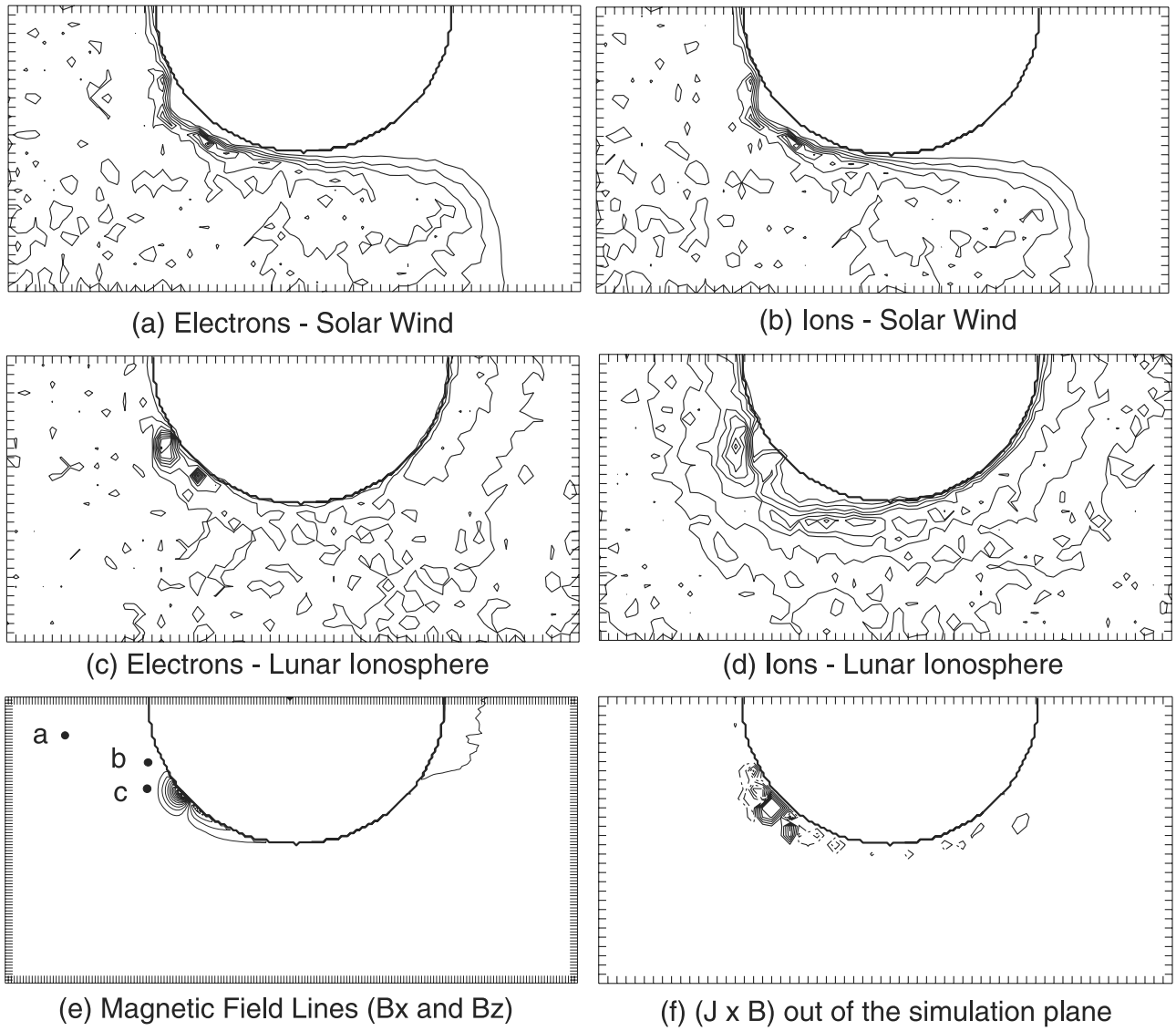

Figure 2. Smoothed density and magnetic field results from particle simulations. Plots (a)–(d) are the density contours for the four particle different populations. Plot (e) is the magnetic field lines for the components in the simulation plane and (f) the Hall component of the electric field in and out of the simulation plane. The contour interval in (a) is 1.1 electrons cm^{-3}, 1.1 ions cm^{-3} in (b), 0.05 electrons cm^{-3} in (c), and 0.02 ions cm^{-3} in (d). All densities are zero in the center of the Moon. The tick marks on the axes of the density plots equal 104.4 km (and 9 grid points) while the tick marks on the axes of the magnetic field line plot are 34.8 km apart. The three spots, and labels, in (e) refer to positions discussed in Figure 6. The thick curve in all the plots indicates the surface.

results. If the magnetopause is defined as the boundary where the solar wind is held off the surface by the anomalous magnetic field, the magnetopause forms at the inner edge of this shock surface. The solar wind ion population penetrates between 12 and 40 km further into the mini-magnetosphere than the electrons, at a variety of positions along the magnetopause. This boundary is also shock-like in that the solar wind electron and ion densities increase by a factor of approximately 3 to 5, as well as being a location of particle acceleration and heating.

[21] The Lunar electrons form two high density regions, one directly above the surface magnetic anomaly, where the magnetic field is the strongest, and one in the downstream region where the anomalous magnetic field is approximately tangential to the surface(Figure 2c). Both regions of enhanced Lunar electron density correspond to density voids in the Lunar ion population (Figure 2d). The region that separates the two enhanced Lunar electron density populations is aligned with a weak density enhancement of Lunar ions. This region of enhanced ions and depleted electrons is near the cusp but not totally aligned with it. A larger density enhancement in the Lunar ion population forms just outside the solar wind shock surface at the subsolar point. Thus the Lunar particles, unlike the solar wind particles, do cross the shock region. The peak of the density enhancement in the Lunar electrons, above the

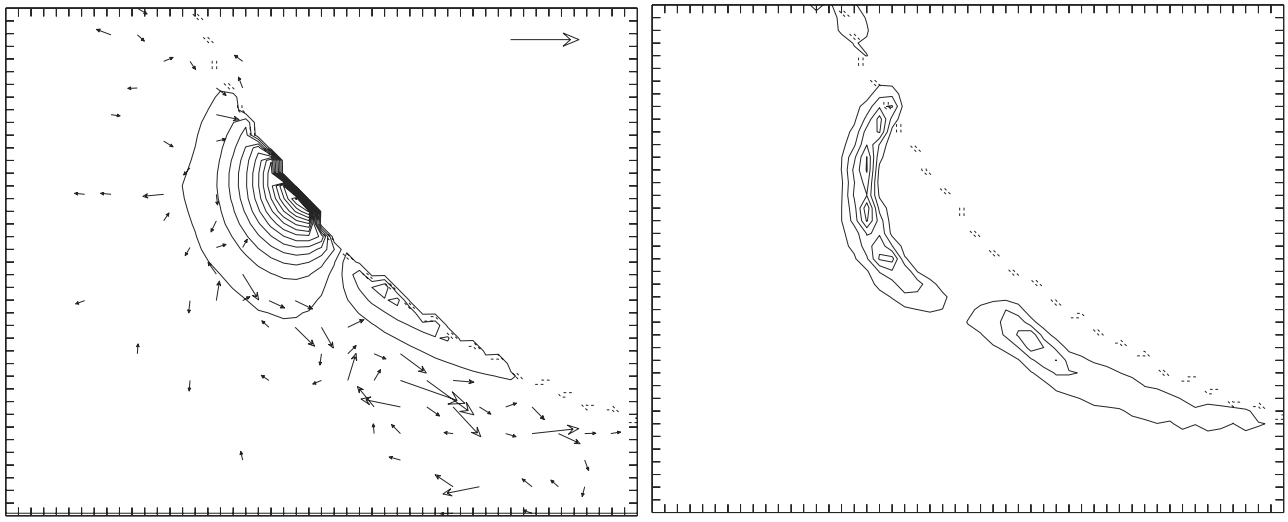

Figure 3. Plots of (a) the flow of the total current in the simulation plane (J_x and J_z), with the magnetic field lines and (b) the magnitude of the total current in and out of the simulation plane (J_y^e) for the simulation presented in Figure 2. The arrow in the upper right hand corner of (a) corresponds to approximately 4000 nA/m^2 and the contour interval in (b) is approximately 8400 nA/m^2. The tick marks are 34.8 km and the plot contains and area 1740 km by 1392 km. The dotted curve indicates the surface of the Moon.

anomaly, occurs in the middle of the solar wind shock surface. And the outer edge of the corresponding Lunar ion density void, coincides with the outer edge of the solar wind shock surface.

[22] That the enhanced Lunar electron densities correspond to regions of high magnetic field indicates the electrons are frozen to the field and act like a fluid. And the fact that the ions, on the other hand, have density voids in regions of high magnetic field suggests that the Lunar ions become demagnetized and cease acting like a fluid.

[23] One question to ask is why the ions leave the mini-magnetosphere when they become demagnetized and why are not they pulled back by Coulomb force from electrons? Space charge fields develop as the solar wind ions and electrons meet the magnetopause. The Lunar ions and electrons respond to this electric field and are able to cross the magnetopause. But the movement of the Lunar electrons across the magnetopause is inhibited by the fact that they are frozen to the magnetic field. The solar wind ions, being the major charge carriers, in addition to having only a small velocity component perpendicular to the magnetic field, must maintain neutrality. Lunar ions and electrons try to short out the electric field and therefore are dragged about but their low density means the electric field is never eliminated.

[24] Signatures of a magnetopause are modified from those seen at the Earth. Instead of two separate density gradients being present at the bow shock and the magnetopause, the density enhancement in each population is a single structure. And instead of the maximum solar wind density being outside of the maximum magnetospheric density, the maximum in Lunar ion density, at the subsolar point, is outside of the enhanced solar wind density and the maximum in the Lunar electron density is in the middle of the solar wind shock. The small size of the mini-magnetosphere leads to a merging of boundaries. Clear separation of the bow shock and magnetopause do not exist as it does in large scale magnetospheres.

[25] The high density region in the downstream Lunar electrons is reminiscent of the stagnation points seen in the previous MHD simulations (locations of high pressure and density but decreased temperature and velocity). The average Lunar electron number density directly above the anomaly is about a factor of 4.5 larger than the value in the solar wind but 6.5 larger in the stagnation region. At the stagnation point the kinetic energy of the electrons is about half the value in the enhanced region directly above the anomaly.

[26] Even at the stagnation point, the mass density of the Lunar electron population is still two orders of magnitude smaller than the solar wind mass density in the shock surface and more than an order of magnitude smaller than the free streaming solar wind density. The velocity of the Lunar electrons is also $1-2$ orders of magnitude smaller than the solar wind velocity. Thus the dynamic pressure of the Lunar electrons is small compared to the dynamic pressure of the solar wind. Inside the mini-magnetosphere, cavities with no Lunar ions form. And the density enhancements in the Lunar ion population only occur outside of the shock surface, both leading to similarly small Lunar ion dynamic pressures inside the shock. Thus the anomalous magnetic field is the only mechanism that can be responsible for holding the solar wind off the surface.

[27] In the Earth's magnetosphere, two distinct current systems occur at the bow shock and magnetopause. In the mini-magnetosphere only one current system occurs inside the bow shock (Figure 3), but with no IMF, a bow shock

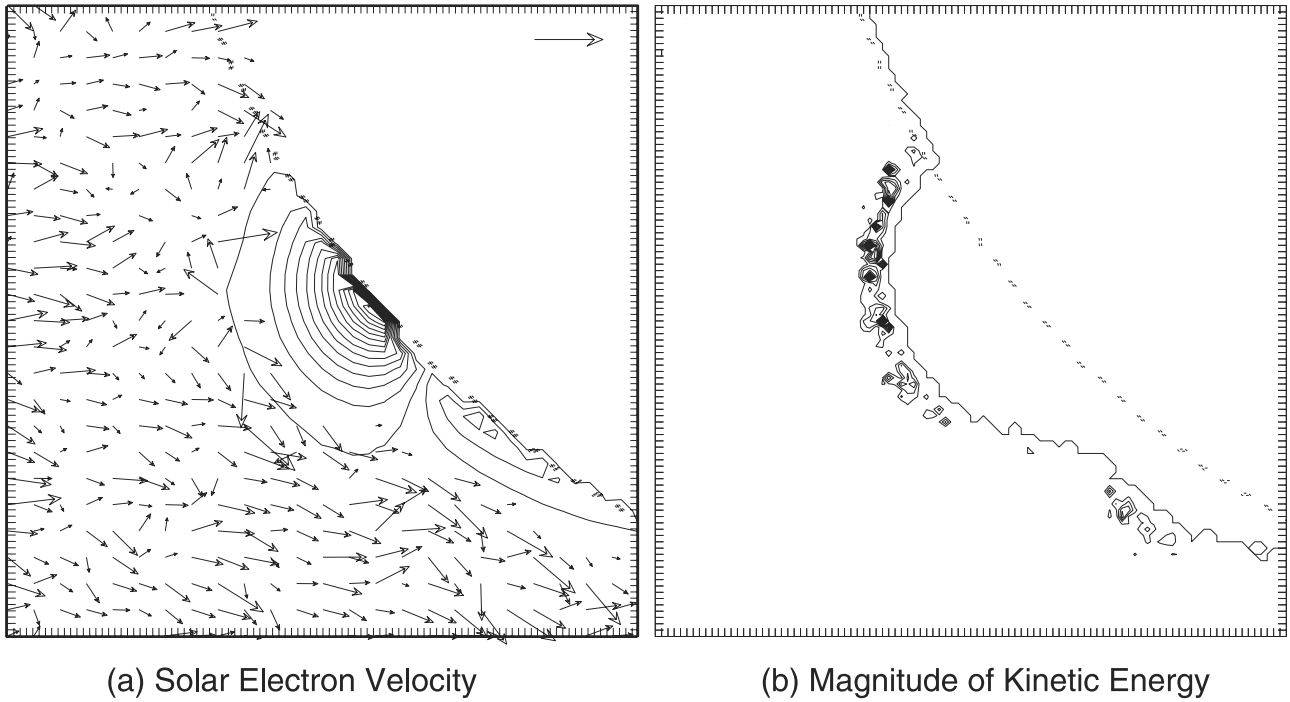

Figure 4. The velocity vectors for the bulk flow (a) and the magnitude of the kinetic energy density (b) for the solar wind electrons for the simulation in Figure 2. The arrow in the upper right corner of (a) indicates a velocity vector with a magnitude of 1075 km/s. The contour interval in (b) is 2.25×10^{-10} Nm^{-3} with the kinetic energy density in the Moon equal to zero. The tick marks on the axes equal 11.6 km in both plots and the boxes contain an area 1160 km by 1160 km. A dotted curve indicates the surface of the Moon.

current system would not form for any sort of magnetosphere. At the magnetopause current system, the maximum dawn–dusk electron current (J_y^e) forms 10–20 km outside of the maximum ion current (J_y^i). The peak ion current is deeper inside the magnetosphere than the peak electron current, as would be expected due to momentum differences and is seen in the Chapman–Ferraro currents at the Earth's magnetopause. The maxima in the dawn–dusk current forms at the boundary between the region of enhanced Lunar ion density and the enhanced solar wind density surface.

[28] Both ion and electron currents are closed by a current system downstream, above the stagnation point. The maximum density in the stagnation point of the Lunar electrons is about 80 km above the surface, with the peak in the associated current system about 150 km off the surface.

[29] In the Earth's magnetosphere, the solar wind particles can be accelerated in the bow shock, but the majority of the flow is diverted around the flanks and heated in the magnetosheath, with the highest temperatures occurring at the subsolar point. In the mini-magnetosphere, boundaries are merged, and heating and acceleration regions form at both the subsolar point and in the downstream flank. Acceleration is seen as an increase in the bulk velocity (Figures 4 and 5), whereas heating appears as spreading of the velocity distribution functions (Figure 6).

[30] The heating and acceleration at the shock surface, directly above the anomaly at the subsolar point, is most prominent in the solar electron particle population. The kinetic energy of the solar electrons (Figure 4) increases by a factor of between 90 to over 200 times the value in the upstream solar wind, while the density increase by only a factor of 4 to 5. The acceleration and heating of solar ions occurs primarily in the downstream region, just above the stagnation point (Figure 5). In the downstream region the kinetic energy of the solar wind ions increases by a more than an order of magnitude, while the density increase by a factor of 3 to 5. The solar wind electrons are also moderately heated and accelerated in the same downstream region as the ions, only further above the surface. The acceleration of the solar wind along the shock surface is not only seen in the increase in the bulk velocity, but also in the presence of both a solar wind ion and electron population traveling upstream.

[31] The largest charge separation of the solar wind at the magnetopause occurs in the downstream region and is due to the electric field generated by the Lunar population. Near the surface there is a net negative charge due to the enhanced Lunar electron density and the density void in the Lunar ions. This electric field draws the solar ions in further at the shock and repels the solar electrons slightly. The largest charge imbalance occurs at the stagnation point. This is an additional source of acceleration for the solar wind ions at the shock surface as well as separating charge more effectively than the momentum difference at the subsolar point.

[32] The total electron distributions show that the bulk flow in the upstream region is slowed while the plasma is heated (Figure 6). Figure 6a is the 2D cuts of the electron

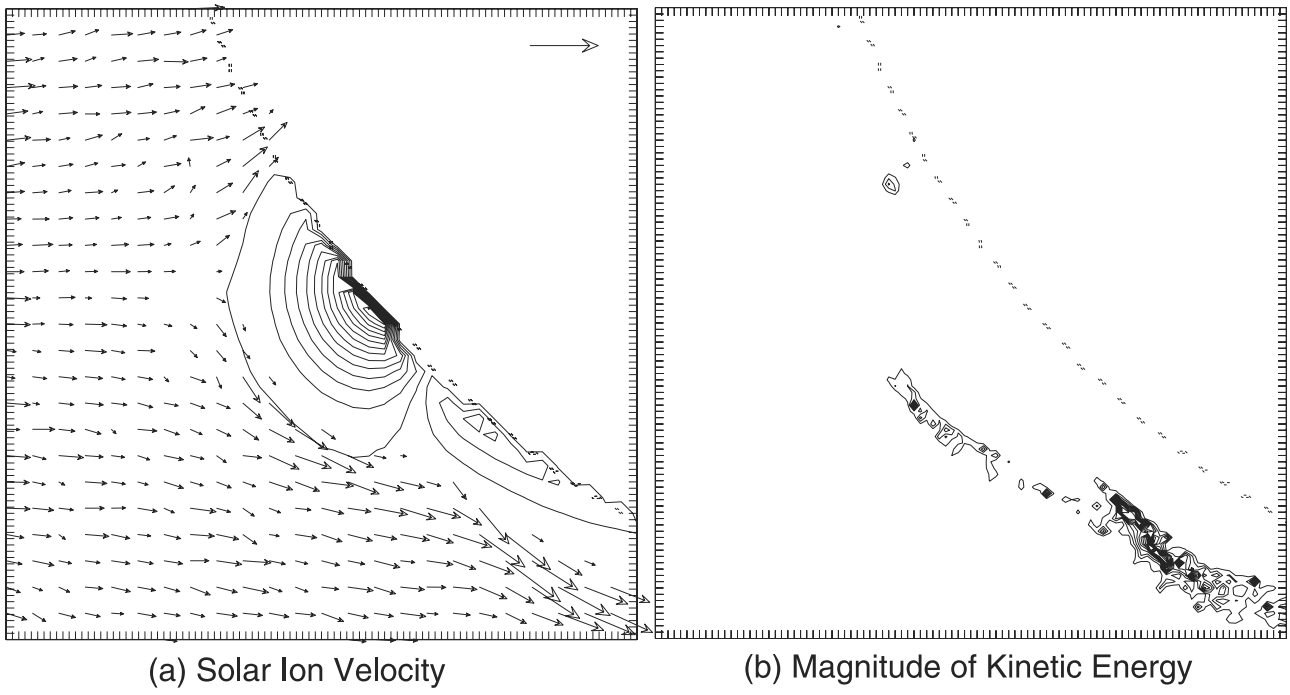

Figure 5. The figure is of the same form as Figure 4 but for solar wind ions. The arrow in the upper right hand corner of (a) has a magnitude of 1231 km/s. The contour interval in (b) is equal to 5.0×10^{-9} Nm^{-3}.

velocity distribution near the edge of the simulation box, where the solar wind enters and is labeled as (a) in Figure 2e. Figure 6b is the velocity distributions from a position 83 km from the surface, and in front of the mini-magnetosphere, parallel to the top edge of the mini-magnetosphere, where the shock attaches to the Lunar surface. Figure 6c is from a point 248 km from the surface, at the outer edge of the solar wind shock surface and directly opposite the dipole. These points are labeled as (b) and (c), respectively, in Figure 2e. Each distribution is for the sum of electrons in a box 580 km (in x) by 348 km (in z) centered about the positions indicated in Figure 2e.

[33] The distribution functions well in front of the mini-magnetosphere (Figure 6a) show an electron population with very little velocity in and out of the simulation plane, and a near Maxwellian distribution with the mean velocity in the simulation plane equal to 400 km/s. The narrow spread of the velocity out of the simulation plane at position (a) is due to the predominate presence of injected solar wind electrons. The solar wind particles are initialized with no velocity out of the simulation plane. The tail in the $-v_x$ direction indicates that the plasma is not completely undisturbed solar wind though, and includes a particle population traveling back upstream. Closer to the mini-magnetosphere, the velocity distributions show significant modification. Not only does the peak of the distributions in the simulation plane decrease to slightly less than 400 km/s in the upper Figure 6b and 200 km/s in the upper Figure 6c, the distributions become much broader, indicating heating of the plasma has occurred.

[34] We can estimate the thermal speed in each direction by determining where the value of the distribution function has fallen to e^{-1} of the peak value. For the distributions in the simulation plane (upper Figures 6a–6c), the thermal velocity in the z direction is between 400 and 500 km/s for all three regions. The thermal velocity in the x direction increase from about 200 km/s in the foreshock region 1, to 400 km/s in region 2, and 600 km/s in region 3.

[35] The particle distributions containing the component of the velocity out of the plane (lower Figures 6b and 6c) show the electrons in the foreshock regions 2 and 3 acquire a velocity in the +y direction. This is primarily due to the solar wind electron population. Position versus velocity plots show that the solar wind electrons are anisotropically heated in the +y direction in the upper half of the shock region and in the −y direction in the lower half of the shock region.

[36] The ion particle distributions show much less modification. The solar wind ions dominate the distributions with a mean velocity of 400 km/s and a thermal velocity on the order of 10 km/s. The ions acquire only a small velocity out of the simulation plane and velocity distribution does not show the same asymmetry that the electron population exhibits near the shock surface (lower Figure 6c).

[37] The only modification in the ion distribution comes in the form of a secondary population. At position (a), the distribution shows a separate population traveling upstream with a velocity of about 250 km/s in the −x direction and 150 km/s in the +z direction, and a thermal velocity of approximately 70 km/s. The ion distribution at (b) is similar with a population traveling upstream with the same velocity in x, but about 250 km/s in the +z direction. And the secondary population is warmer with a thermal velocity on the order of 100 km/s. At (c) the mean velocity of the secondary population in the z direction is zero, while the peak in the velocity distribution in x spreads between 200

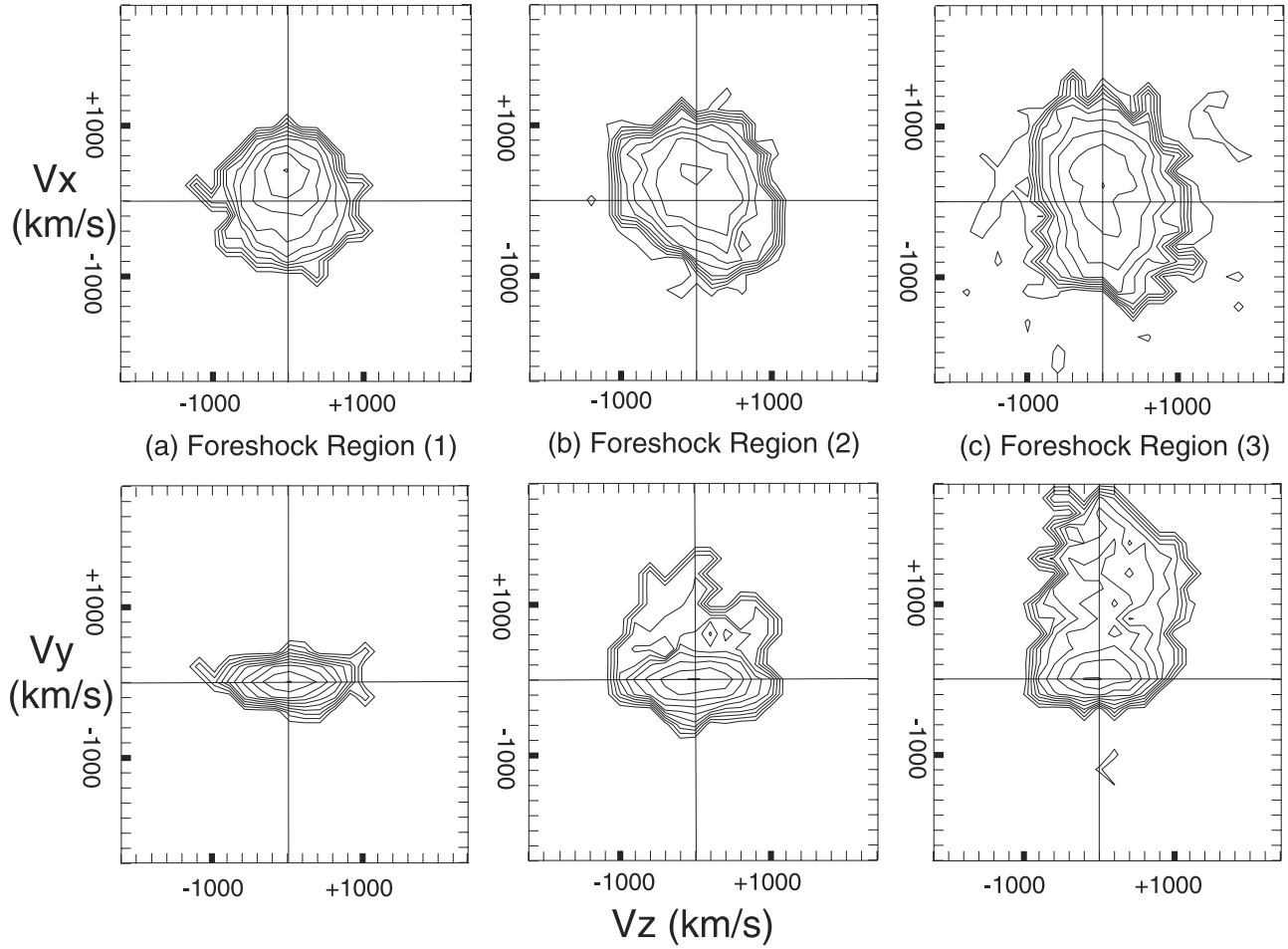

Figure 6. The total electron velocity distributions for three regions outside of the mini-magnetosphere in Figure 2. Each distribution is for the sum of electrons in a box 580 km (in x) by 348 km (in z) centered about the positions indicated with a spot and a label in Figure 2e. Figure (a) is in the foreshock region, near the edge of the simulation box. The distribution in (b) is from a region approximately 83 km from the surface, in front of the upper edge of the shock region where the shock connects to the Moon just above the anomaly. Figure (c) is the distribution from approximately 248 km from the surface, in front of the shock region and directly opposite the anomalous region. The upper plots are the velocities in the simulation plane (v_x and v_z) and the lower plots contain the velocity out of the simulation place (v_y and v_z). The tick marks on the axes equal 200 km/s, and the cross hairs indicate zero.

and 400 km/s, with a thermal velocity on the order of 200 km/s. These results are all consistent with a plasma being heated at a shock and a portion of the population reflected back upstream.

[38] When the bulk velocity of the solar wind was decreased by 58%, the size of the mini-magnetosphere nearly doubles (Figure 7). The initial thermal velocities in Figures 2 and 7 are identical, but the bulk velocity of the solar wind was decreased from 400 km/s in Figure 2 to 165 km/s in Figure 7, translating to an increase in the surface magnetic field strength to approximately 200 nT. All other quantities, such as mass ratios, remain the same. The result is a mini-magnetosphere that is more than 100% larger, with the magnetopause moving out from 160 km to approximately 400 km above the surface. A very large stagnation point develops downstream in the Lunar electron population, but there are no clear Lunar ion plasma voids corresponding to the enhanced electron density regions. The Lunar electron density enhancements are similar in shape to the case with the higher bulk speed, but about 10% smaller in magnitude.

[39] The particle distributions show much less heating, particularly in the case of the electrons. The electron distributions containing the velocity component out of the simulation plane indicate the presence of anisotropic heating is similar to, but not as large as, the heating in the lower panels in Figure 6. And with the inflated shock surface (Figure 7b), position (b) in Figure 2 is now in the solar wind shock, while position (c) is inside the magnetopause. The thermal velocities for the cases in Figures 2 and 7 are similar in the foreshock region 1. At position (a), a particle population traveling upstream is still present but the tail of the distribution is much smaller. This is not due to fewer particles traveling upstream, but rather the particles traveling upstream have a smaller velocity. Inside the shock region (positions (b) and (c)), the mean velocity is zero, while the thermal velocity in the simulation plane is approximate 350 km/s at both positions.

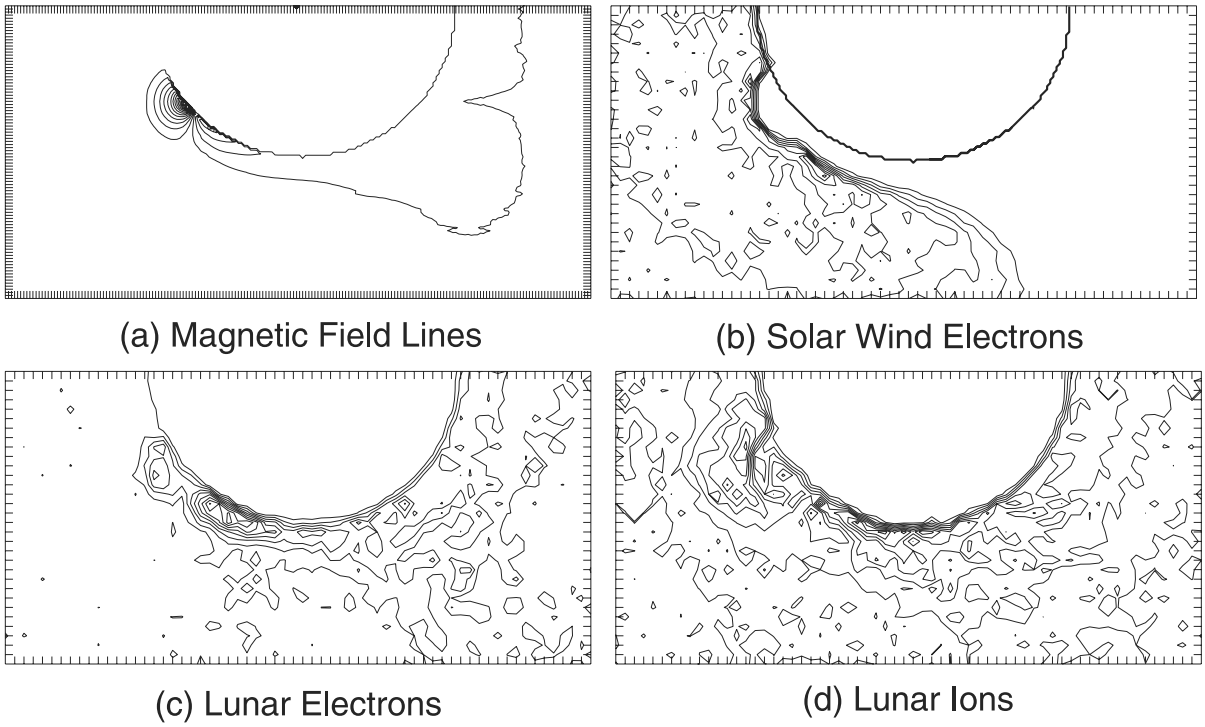

Figure 7. Magnetic field lines and density contours for the simulations with decreased bulk velocity of the solar wind. The Lunar ion to electron mass ratio was set equal to 1024, while the bulk velocity of the solar wind was equal to 165 km/s. The particle temperatures are equal to those in Figure 2, at 0.02 eV for the Lunar electrons and ions, and 2.22 eV for the solar wind electrons and ions. The contour interval in (b) is 0.88 electrons cm^{-3}, 0.05 electrons cm^{-3} in (c), and 0.014 ions cm^{-3} in (d), with the densities in the center of the Moon equal to zero. The density plot for solar wind ions looks nearly identical to (b). All plots are of the same form as those in Figure 2.

[40] When the thermal and bulk velocities were increased by an order of magnitude from the conditions in Figure 7, a shock-like structure still occurs but solar wind particles can penetrate all the way to the surface of the Moon. The bulk velocity translates to an ion gyroradius of 255 km and an anomalous magnetic field strength at the Lunar surface of 15 nT, too weak to hold off all of the solar wind. A shock-like structure is still present but significantly closer to the surface. Regions of enhanced Lunar electrons and depleted Lunar ions are still present though.

[41] In all three simulations shown in Figure 8, the bulk velocity of the solar wind was equal to 1622 km/s. The initial temperature of the solar wind was set equal to 220 eV, while the temperature of the Lunar particles is 1.70 eV. The only difference in the three simulations in Figure 8 is the mass ratio of the Lunar ions to electrons, and consequently the solar wind ion to Lunar ion ratio.

[42] The Lunar ion to electron mass ratio had little effect on the size and shape of the mini-magnetosphere, when all other variables were held constant. The mass ratio was set to 1024 in Figure 8b, 256 in Figure 8c, and 64 in Figure 8d to simulate 3 different ion populations, Argon, Neon and Hydrogen, respectively. Thus the solar wind ion to Lunar ion mass ratio is equal to 4.375 in Figure 8b, 17.5 in Figure 8c, and 70 in Figure 8d. The magnetic field lines in Figure 8a are for the simulation with a Lunar ion to electron mass ratio of 1024, but are nearly identical to the magnetic field in the simulations with the other 2 mass ratios.

[43] The confinement of the Lunar electrons and a void in Lunar ions above the anomalous region is present in all three simulations, as in the first case (Figure 2) where the surface inside the mini-magnetosphere is completely shielded from the solar wind. No stagnation point is present though. A shock-like structure forms in the solar wind population above the anomaly. The solar wind density enhancement at the shock is about 40% that in Figure 2, while the Lunar electron density enhancement is slightly larger. The velocity distribution functions near the region show heating and acceleration signatures similar to those near the larger mini-magnetosphere in Figure 7.

3. 2.5D MPD Simulations

3.1. Model Parameters

[44] The results from the particle simulations further accentuate the need to extend the ideal MHD model to incorporate small-scale and nonideal MHD effects, like those incorporated by *Winglee* [1994]. Charge separation occurs in the Lunar particle populations and nonideal MHD behavior is seen in a Hall component of the electric field which is nonzero and an ion population which becomes demagnetized.

[45] The following fluid equations are solved numerically:

$$\frac{\partial \rho}{\partial t} + \nabla \cdot \vec{m} = 0 \tag{3}$$

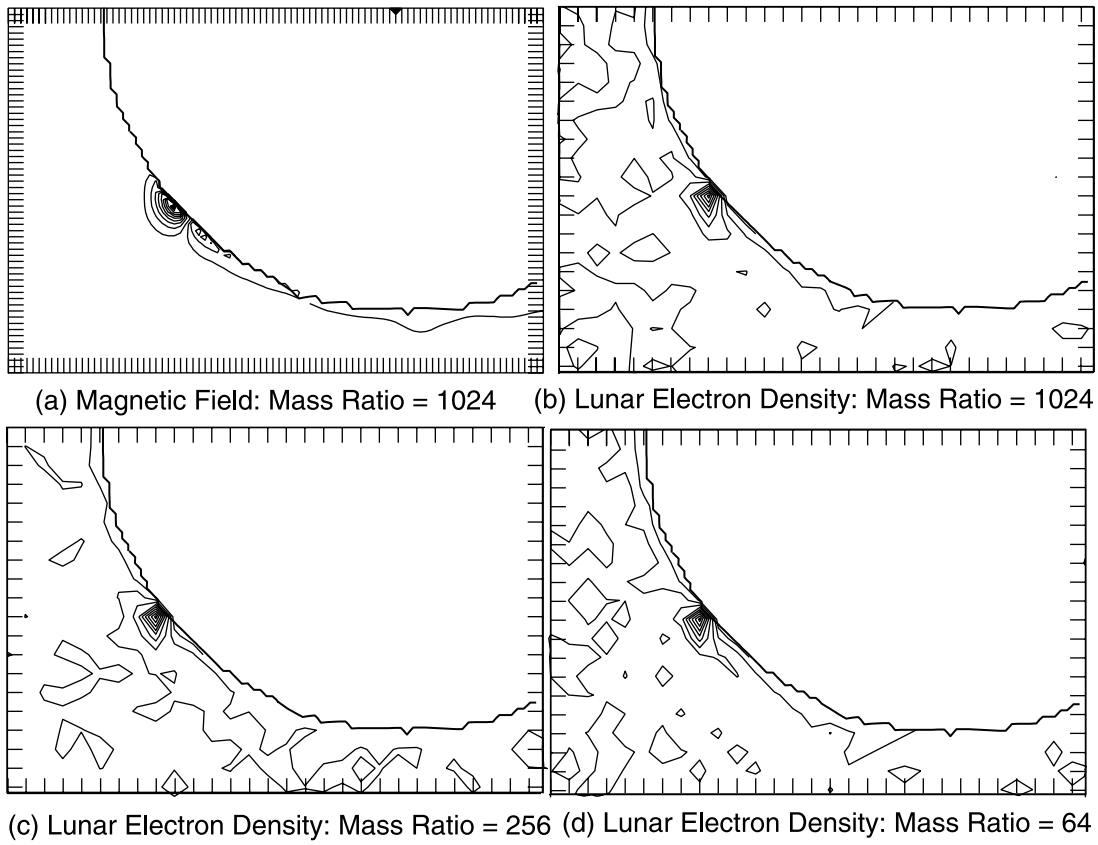

Figure 8. Lunar electron densities for simulations with the Lunar ion to electron mass ratio equal to (b) 1024, (c) 256, and (d) 64 and magnetic field lines (a) for mass ratio equal to 1024. The bulk and thermal velocities are an order of magnitude larger than those in Figure 7. The bulk speed of the solar wind was equal to 1622 km/s. The temperature of the Lunar electrons and ions is 1.70 eV, while the temperature of the solar wind electrons and ions is 220 eV. The contour interval in both (b) and (d) is 0.05 electrons cm^{-3}, and 0.06 electrons cm^{-3} in (c). All plots contain an area of 2088 km by 3027.6 km and are of the same resolution as those in Figure 2. The thick curve has been added to indicate the surface.

$$\frac{\partial \vec{m}}{\partial t} + \nabla \cdot \left(\vec{m} \frac{\vec{m}}{\rho} \right) + \nabla P = \vec{J} \times \vec{B} \tag{4}$$

$$\frac{\partial \mathrm{e}}{\partial t} + \nabla \cdot \left(\frac{\vec{m}}{\rho} (\mathrm{e} + \mathrm{P}) \right) = \vec{\mathrm{E}} \cdot \vec{\mathrm{J}} \tag{5}$$

$$\frac{\partial \vec{B}}{\partial t} - \nabla \times \vec{E} = 0 \tag{6}$$

$$\vec{J} = \nabla \times \vec{B} \tag{7}$$

Accounting for regions of nonideal MHD behavior and regions of localized nonneutrality simply means that Ohm's Law is of the form:

$$\vec{E} = -\vec{v} \times \vec{B} + \eta \vec{J} + \frac{c}{\omega_{pi} \mathrm{Lr}} \left(\vec{J} \times \vec{B} - \nabla P_e \right) \tag{8}$$

$\vec{E}$ is the electric field, $\vec{B}$ is the magnetic field, $\vec{J}$ is the current density, P_e is the electron pressure (and equal to half the total pressure, P), e is the energy, $\vec{m}$ is the momentum, ρ is the density, η is resistivity, c is the speed of light, L is the scale size of the grid in the simulation, and ω_{pi} is the hydrogen ion plasma frequency. The resistivity (η) is set to zero outside of the Moon and the Hall and ∇P_e terms are only evaluated outside of the Moon. Like the 2.5D particle simulations, the vector quantities are three component vectors, but the spatial derivatives are only taken in two dimensions.

[46] *Sonnet* [1975] placed the Lunar resistivity between 10^3 ohm m and 10^5 ohm m. The Lunar resistivity in the simulations (η) is set to 10^4 ohm m. This allows the magnetic field to diffuse through the Moon and not cause an unphysical pile-up of the IMF at unmagnetized surfaces, while simultaneously not causing the simulation to go unstable [*Harnett and Winglee*, 2000]. The corresponding Reynolds number inside the Moon is ~0.10.

[47] Numerical uncertainty leads to a numerical resistivity and can cause diffusion of the magnetic field even in regions where η is set to zero. The Reynolds number associated with the numerical resistivity is on the order of 50,000 in the solar wind, and an order of magnitude smaller in the mini-magnetosphere, indicating that diffusion of the magnetic field outside of the Moon is negligible, and collisionless behavior dominates.

[48] Since the particle motions are fundamentally small in MHD, the value of $c/(\omega_{pi}L)$ must be set to a fraction of it

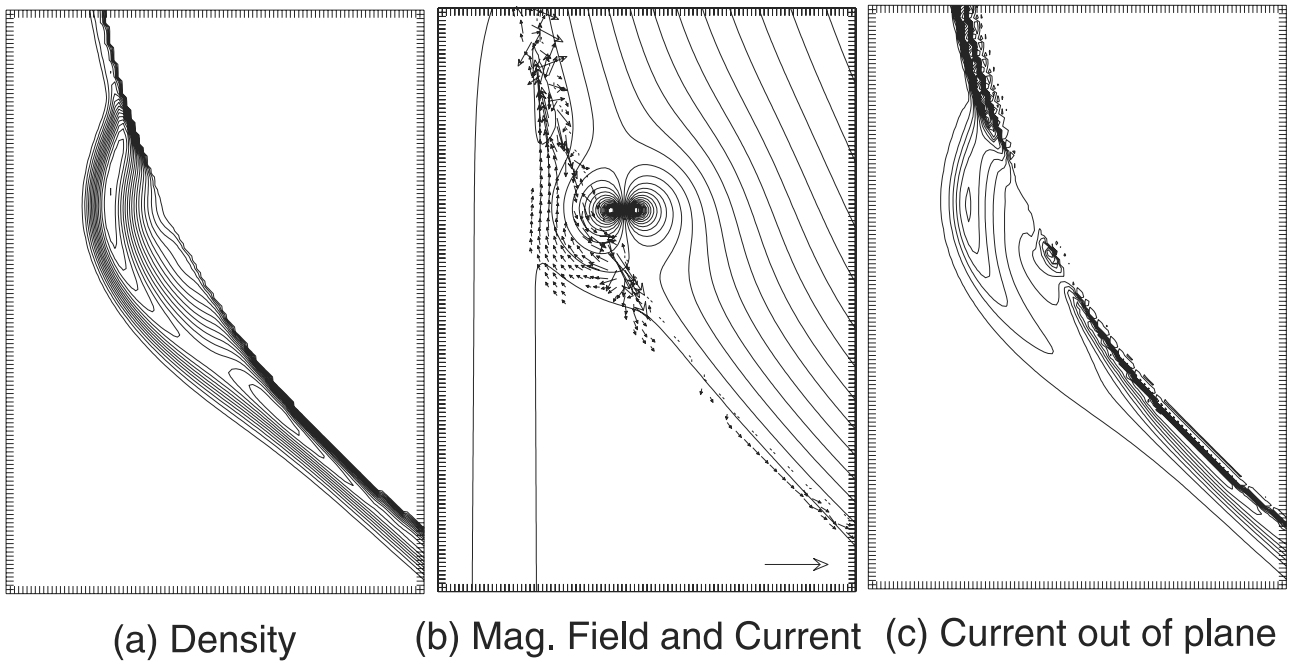

Figure 9. The (a) fluid density, (b) the magnetic field lines with the current density in the simulation plane and (c) the current density out of the simulation plane (c). The effective dipole moment is in the $+\hat{z}$ direction, antiparallel to the IMF. The tick marks on the axes are equal to 8.7 km and the boxes contain and area 870 km by 1218 km. The contour interval in the density plot is equal to 2.1 ions cm^{-3}, with the density in the solar wind equal to 10 ions cm^{-3}. The arrow in the lower right hand corner of (b) indicated a current density magnitude of 53.9 nA/m^2. The contour interval in (c) is 129.7 nA/m^2, with the current density in the solar wind approximately zero. The dotted line in plot (b) indicates the surface of the Moon.

value. The full value, equal to 2.07, will cause the simulation to go unstable. For these MPD simulations, $c/(\omega_{pi}L)$ was set at a value of 0.10, with a value larger than 0.12 causing the code to go unstable. The larger the ratio is, the stronger the particle type effects. In the simulations by *Winglee* [1994], $c/(\omega_{pi}L)$ was set equal to 0.125. Including the extra terms in Ohm's Law allows for currents and electric fields in the simulation plane, as well as magnetic fields and velocity in and out of the simulation plane. The remainder of the fluid model is explained by *Harnett and Winglee* [2000].

[49] The simulations with the modified Ohm's Law were run with the same initial conditions as the previous MHD simulations without the Hall and ∇P terms [*Harnett and Winglee*, 2000]. The solar wind was assumed to be composed of H^+ ions with a density of 10 ions cm^{-3} and a velocity of 400 km/s. The Lunar density was assumed to be 0.1 Ar^+ ions cm^{-3} on the day side and 0.01 on the night side. The MPD simulations are a one ion population fluid code so an Ar^+ ion is treated as 40 H^+ ions.

[50] The pressure and temperature of the solar wind are equal to 0.02 nPa and 12 eV. The IMF is set to 2.5 nT in the southward direction ($-\hat{z}$). Larger IMF strengths would not diffuse sufficiently fast through the Moon and would cause unphysical pile-up of the IMF at the unmagnetized surfaces [*Harnett and Winglee*, 2000]. The anomalous dipole magnetic field was created with two opposing current elements placed just below the surface at 26.1 and 78.3 km below the surface, respectively. This creates anomalous magnetic field strength equal to 30 nT at 100 km above the surface, when the surface field strength is set to 290 nT. Only the direction of the effective dipole moment was varied in the simulations.

3.2. Fluid Model Results

[51] In Figure 9 the effective dipole moment of the anomalous region points in the northward ($+\hat{z}$) direction, thus the surface magnetic field points in the same direction as the IMF. The addition terms in Ohm's Law allow for additional currents and electric fields but cause no change in shape of the mini-magnetosphere. The internal structure of the density and pressure inside the mini-magnetosphere is altered slightly, with the maxima pressure, densities and temperatures reduced by about 10%. This is due to a slightly smaller time step in the simulations, which translates to a slight increase in numerical diffusion of the magnetic field in the plasma. With increased numerical diffusion of the magnetic field in the mini-magnetosphere, the plasma will not build up as much. The shape of the shock surface remains the same but due to the reduced internal pressure, density and temperature the shock height moves in about one grid point. The stagnation point occurs at the same location as in the 2D MHD simulations, about 540 km downstream.

[52] The current density (Figure 9b) in the simulation plane near the anomaly is field aligned in most regions. The magnitude of the current density in the simulation plane is about an order of magnitude smaller than the current out of the simulation plane in the shock region. Above the anomaly, the current density forms a circulation pattern. The region that separates currents traveling in opposite direc-

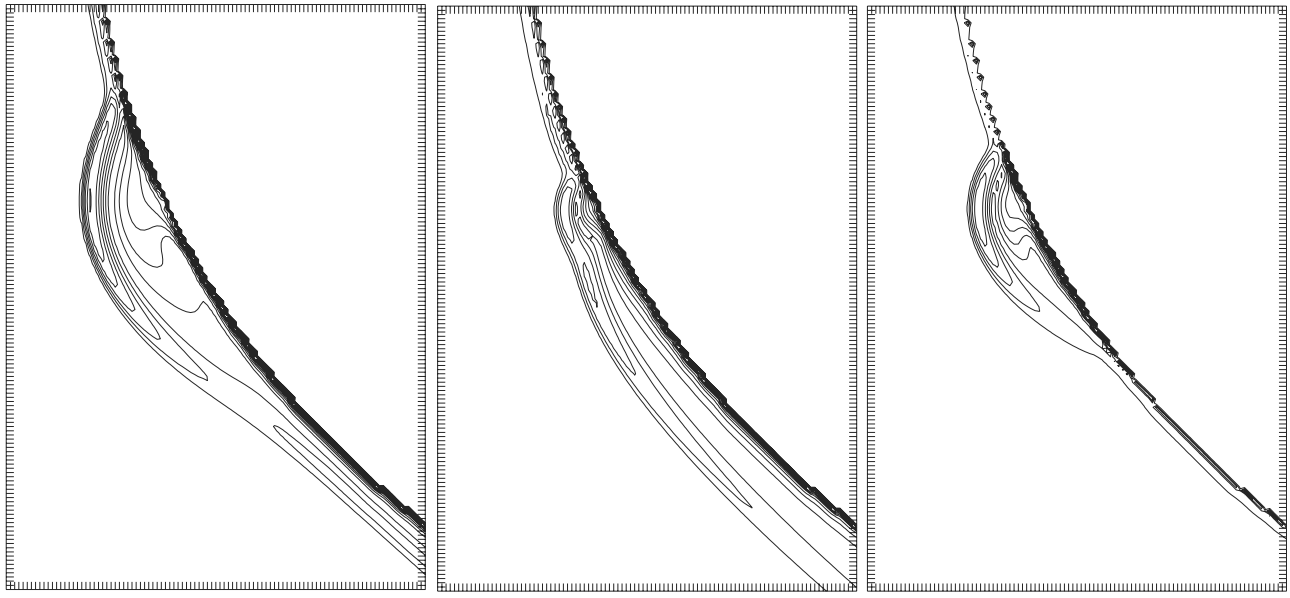

Figure 10. The magnitude of the pressure gradient (∇P) component of the electric field for the cases when (a) the dipole moment is antiparallel to the IMF (Figure 9), (b) the dipole moment is parallel to the IMF (Figure 12), and (c) the IMF is zero (Figure 13). The contour interval in (a) is 64.4 μV/m, 94.8 μV/m in (b) and 78.6 μV/m in (c). The boxes are of the same forms and size as in Figures 9, 12, and 13.

tions is in the density gradient near the surface, inside of the density maxima and approximately 70 km above the surface when directly opposite the location of the dipole generating current elements. These plasma surface currents are created by the charge separation at the magnetopause. The electrons are stopped first by the anomalous magnetic field and move with the bulk flow down and around the anomaly, creating a current in the upward direction. The ions penetrate further into the mini-magnetosphere before being deflected down and around, creating a current in the downward direction.

[53] The electric field in the simulation plane is significant only at the edge of the shock surface, where it points into the solar wind, and in the inner portion of the mini-magnetosphere directly opposite the buried dipole, where is points toward the surface. The electric field at the shock surface is primarily the result of a strong pressure gradient (Figure 10a), further indicating the presence of charge separation. Solar wind ions are able to penetrate further into the mini-magnetosphere, creating the electric field at the shock surface, pointing into the solar wind.

[54] The electric field pointing toward the surface suggests an excess of electrons near the surface and/or a deficit of ions. The pressure gradient (Figures 10a) is significant in the region directly above the anomaly, but its effect on the electric field is reduced by a Hall field (Figure 11a) in the opposite direction. The charge separation in this region is the result of the nonideal MHD behavior, seen in the nonzero Hall field (Figure 11a). The velocity of the plasma inside the shock, opposite the anomaly, is small. Therefore charge separation would not be the result of the momentum difference in the ions and electrons that leads to the charge separation at the shock surface. Also such mass effects would create an electric field in the opposite direction of the one present at the surface. Instead the nonideal plasma behavior leads to a deficit of ions relative to the electron density. Since there is a relative deficit of ions where both the plasma density and magnetic field increase, it suggests the ions have become demagnetized, and are no longer frozen to the magnetic field as a fluid. That the Hall and pressure gradient terms are nonzero throughout the mini-magnetosphere, but cause little modification of the shape and size of the mini-magnetosphere indicates that the bulk characteristics of the mini-magnetosphere are determined largely by fluid behavior.

[55] When the direction of the effective dipole moment of the anomalous magnetic field is flipped (to $-\hat{z}$), the size and shape of the mini-magnetosphere changes dramatically due to interactions with the IMF (Figure 12), as was seen in the previous 2D MHD simulations. Near the anomaly, the pressure, density and temperature are again reduced by about 10% from the 2D simulation due to the smaller time step. As a result the shock height is one grid point lower directly above the anomaly.

[56] The electric field in the simulation plane is occurs primarily at the shock surface. Only a weak electric field points toward the surface above the anomaly. This is due to the increase in the Hall term. Both the Hall term and space charge field (associated with the pressure gradient) in the region directly opposite the anomaly have increased from the case in Figure 9 but the Hall term increases by a larger percentage (the magnitude of the space charge field is double while the Hall term magnitude is triple the corresponding terms for the case in Figure 9). Thus near the anomaly, both charge separation and nonideal MHD behavior are more prevalent than in the previous case, even though the electric field is smaller.

[57] The direction of the anomalous magnetic field at the surface is in the opposite direction as the IMF. This allows

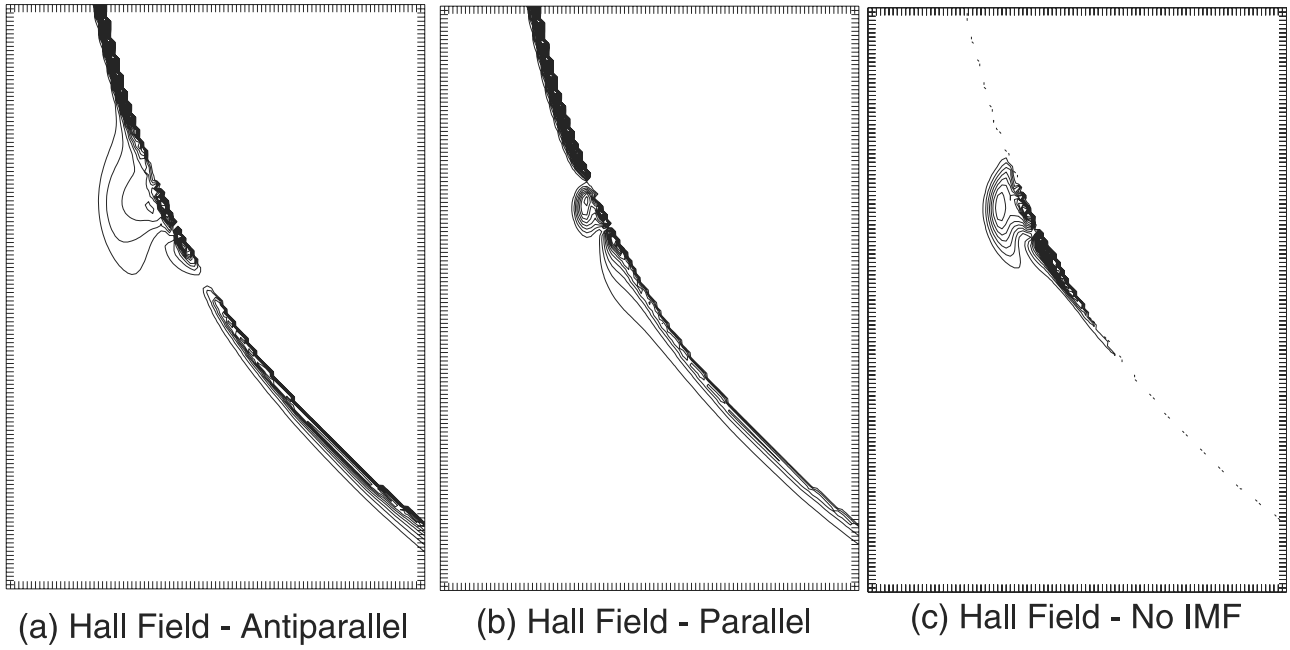

Figure 11. The magnitude of Hall ($\vec{J} \times \vec{B}$) component of the electric field for the cases when (a) the dipole moment is anti-parallel to the IMF (Figure 9), (b) the dipole moment is parallel to the IMF (Figure 12), and (c) there IMF is zero (Figure 13). The contour interval in (a) is 77.4 μV/m, 118.4 μV/m in (b) and 66.3 μV/m in (c). The boxes are of the same forms and size as in Figures 9, 12, and 13. The dotted line in (c) indicates the surface of the Moon.

for wide scale reconnection. As a result there is fluid flow into the cusp-like regions. Large currents are associated with this flow into the cusp regions. The current density (Figure 12b) in the cusp regions are approximately 1.5 times larger than the largest currents seen in Figure 9b. The surface plasma currents opposite the anomaly in Figure 12b are approximately 2.5 times larger than the currents in the same location in Figure 9b but still about half the magnitude the

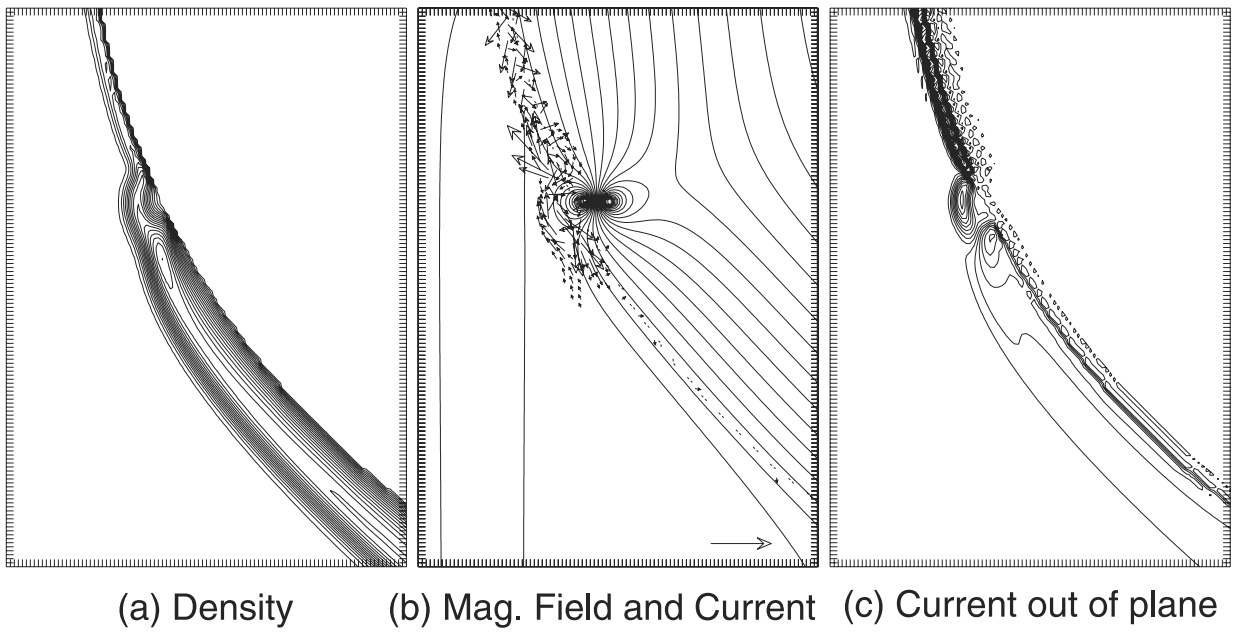

Figure 12. The effects of flipping the effective dipole moment from $+\hat{z}$ to $-\hat{z}$, now parallel to the IMF. The plots are of the same form and scale as in Figure 9. The contour interval in the density plot is equal to 2.0 ions cm^{-3}, with an interval of 171.8 nA/m^2 for the current density. The magnitude of the reference arrow in (b) is 65.1 nA/m^2.

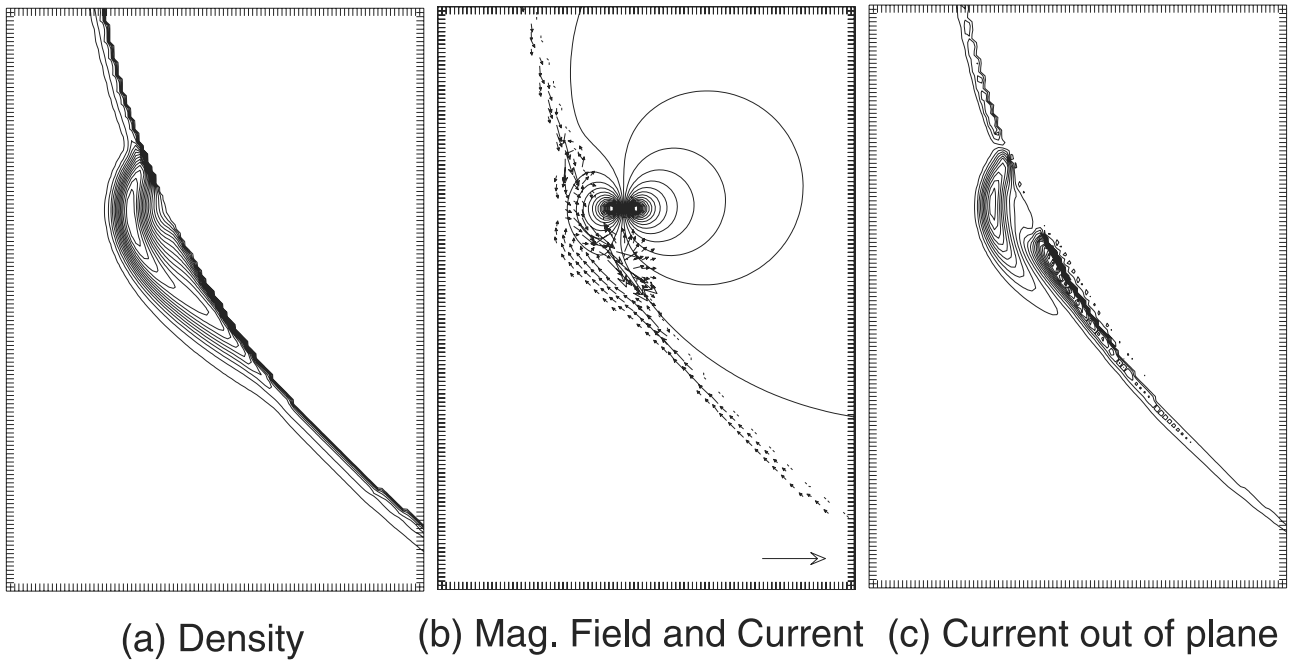

Figure 13. The effects of no magnetic field in the solar wind. The plots are of the same form and scale as in Figure 9. The contour interval in the density plot is equal to 1.6 ions cm^{-3} and 114.1 nA/m^2 for the current density out the plane. The magnitude of the reference arrow in (b) is 91.3 nA/m^2.

cusps currents. Thus the circulation pattern in the charge density associated with charge separation at the magnetopause is present but occurs over a more compressed region, leading to larger current densities. The surface plasma current is still an order of magnitude smaller than the current density out of the simulation plane, due to the overall increase in the magnitude of the current near the anomaly.

[58] The direction of the current relative to the fluid velocity in the cusps suggests that the large cusp currents are due to electron precipitation. The fluid flow is down to the surface while the current is out from the surface. Large currents out of the Earth's ionosphere can occur in the nightside auroral zone during an auroral event. These currents are associated with electron precipitation into the auroral zone and are typically associated with southward IMF. The large currents in the cusp of the mini-magnetosphere are only present in the configuration that is analogous to southward IMF configuration for the Earth (Figure 12).

[59] It was noted previously [*Harnett and Winglee*, 2000] that the internal structure of this mini-magnetosphere (Figure 12) approached the size of the ion gyroradius. One might expect that the largest modification to the mini-magnetosphere by the nonideal MHD terms would come in such a case. Directly above the anomaly the magnitude of the Hall field (Figure 11b) does have a maximum value approximately 3 times larger than that in the larger mini-magnetosphere (Figure 11a), but the Hall field is nonzero over a much smaller region due to the smaller size of the mini-magnetosphere. Thus while the nonideal MHD effects are stronger, they occur over a much smaller area within the mini-magnetosphere leading to little change from the ideal MHD simulations.

[60] To make a more compatible comparison between the MPD simulations and the particle simulations, the IMF needs to be set to zero in the MPD simulations (Figure 13). With no IMF, the mini-magnetosphere is very round and no stagnation point develops. The mini-magnetosphere is nearly identical to the mini-magnetosphere that formed in the ideal 2D MHD simulations [*Harnett and Winglee*, 2000] when the IMF was set to 5 nT in the ecliptic plane and B_z was set to zero. The shock height directly opposite the buried dipole for both cases is 130 km even though the maxima pressure, density and temperature are approximately 5% smaller for the MPD simulation with no IMF due to the decreased time step.

[61] The lack of B_z results in a smaller mini-magnetosphere, with less build-up of pressure and density. The maximum temperature is the same as the case in Figure 9, but the maxima in pressure and density are smaller in the case with no IMF. With no IMF the magnetic field of the anomaly is compressed but fluid can flow around the anomaly unimpeded by IMF. This is evident in that no stagnation point forms when the IMF is zero. Reconnection of the IMF to the anomalous magnetic field can lead to regions of inhibited fluid flow and the development of stagnation points, increasing the pressure and density.

[62] The magnitude of the Hall field (Figure 11c) directly opposite the anomaly is roughly 1.5 times larger than for the case in Figure 11a, but about half the value in Figure 11b. It is nonzero throughout a larger percentage of the mini-magnetosphere, since the Hall field is minimal in the flank/tail region of the mini-magnetosphere in Figures 9 and 12, as those regions are associated with solar wind flow. Thus the smaller the mini-magnetosphere, the more prevalent the nonideal MHD behavior.

[63] Substantial currents also form near the lower cusp-like region in the case with no IMF and are larger than those in the previous case (Figure 12), but the direction of the

current is not the same. In the previous case, the large currents are directed out of the cusp. But in the case with no IMF, the large currents are tangent to the Lunar surface and in the direction of the bulk flow, suggesting they are associated with a compressed region of ion flow. The upward currents associated with the downward electron flow are comparable in magnitude to those in Figure 12b.

4. Comparison Between Particle and MPD Simulations

[64] The rounded shape of the mini-magnetosphere and magnetic field geometry is similar in the particle simulations and the MPD simulations where large scale reconnection to the IMF does not occur. And the topology of the Lunar electron density is very similar to the density topology in Figures 9 and 13. Both types of simulations have large density concentrations directly between the solar wind and the magnetic anomaly, and for some cases in the MPD simulations, in the downstream region as well. While a stagnation point is present in some of the particle simulations (where the IMF is zero), no stagnation point is present in the fluid simulations if B_z is zero. A stagnation point is present in the MPD simulations only when B_z is nonzero.

[65] The cusps form a possible entry point for solar wind plasma to reach the surface. Flow into the cusp is seen in the fluid simulations, and in the southward IMF configuration electron precipitation into the cusps generates large currents. The velocity and density in the particle simulations, on the other hand, indicate there is no flow into the cusp by the solar wind for the strong magnetic field cases (Figures 2 and 7), as the solar wind ions and electrons are completely deflected by the magnetic anomaly.

[66] The solar wind in the particle simulations is accelerated, as well as heated, as it encounters the shock region. These regions are most prominent at the subsolar point for the solar wind electron population and in the flank region for the solar wind ion population. The acceleration is evident as an increase in the bulk velocity. The effects of heating appear as spreading of the velocity distribution functions. The fluid in the MPD simulations is heated, but the bulk flow is never accelerated above the initial solar wind speed. This is inherent to MHD/MPD, as it can not predict the production of high energy tails in the velocity distribution.

[67] An electric field, due to the pressure gradient, pointing into the solar wind at the shock surface in all of the MPD simulations indicates the presence of charge separation at the shock surface and that the ion population of the solar wind penetrates further into the mini-magnetosphere than the electrons. The solar wind in the particle simulations also exhibits a similar charge separation at the subsolar point. Charge separation of the solar wind in the particle simulations also occurs in the downstream region, near the stagnation point.

[68] Charge separation of the Lunar population in the particle simulations also occurs at the subsolar point. This excess of electrons and deficit of ions seen in the Lunar population of the particle simulations creates an electric field similar to one in the MPD simulations. An electric field pointing toward the surface, due to a nonzero Hall field and a pressure gradient, indicates a deficit of ions relative to the electron density near the surface in the MPD simulations. Since the charge separation occurs where the momentum of the plasma is small, it must be due to nonideal MHD behavior, rather than mass separation like that which occurs at the shock surface. Thus the MPD simulations can capture both the charge separation and ion demagnetization that is seen in the particle simulations.

[69] This region of enhanced electrons and a void of ions encompasses the entire mini-magnetosphere in the particle simulations. The magnitude of the Hall field in the MPD simulations is large near the surface directly above the magnetic anomaly, but small in the downstream region of mini-magnetosphere. The region of charge separation near the surface is large relative to the size of the mini-magnetosphere only in the case with no IMF, where the scale size of the mini-magnetosphere is small. Thus the ions in the MPD simulations only become demagnetized directly opposite the anomaly. This is due to not incorporating the full strength of the particle effects, seen in the reduced value of $c/(\omega_{pi}L)$ in Formula 8.

[70] A circulation pattern in the current, due to momentum (thus charge) separation at the magnetopause, is seen in both the particle simulations (Figure 3a) and the MPD simulations (Figures 9b, 12b, and 13b) but is most prominent in the downstream in the particle simulations rather than above the anomaly as in the MPD simulations. In the particle simulations there is charge separation of the solar wind at the subsolar point but it is minor compared to the charge separation in the downstream region. Thus the largest currents in the simulation plane occur near in the downstream region.

[71] Magnetopause currents form at the bow shock in both particle and MPD simulations. Additional currents out of the plane form in both types of simulations but not at the same location. In the MPD simulations, the downstream current forms around the cusp and near the surface (Figures 12c and 13c) while in the particle simulations, the additional current out of the plane is in the flank region past the cusp (Figure 3b), and above the stagnation point. This is due the lack of IMF in the particle simulations and the fact that the solar wind is completely held off the surface and deflected around the magnetic anomaly. In both cases the current is due to the electric field associated with the flow of solar wind ions across the Lunar magnetic field (i.e., $E = -v_{solar} \times B_{Moon}$).

[72] The currents in the MPD simulations are similar to the plasma surface currents seen at the Earth's magnetopause in simulations by *Winglee* [1994]. In both cases, the surface currents are approximately an order of magnitude smaller than the magnetopause current in the dawn–dusk direction. Only one current system forms in the bow shock-magnetopause region in the MPD simulations, even with a nonzero IMF, rather than a separate current system at each boundary. Therefore the general appearance of the current is similar to the particle simulations where no IMF is present. This suggests that the current systems are compressed even in the conditions when a separate bow shock current might form. Like the MPD simulations, the current out of the plane in the particle simulations is an order of magnitude larger than that in the plane.

[73] The Hall field out of the simulation plane in the particle simulations is nonzero throughout most of the

mini-magnetosphere (Figure 2f). In the MPD simulations the component of the Hall field out of the simulation plane is nonzero only very near the anomaly. But the components in the simulation plane are nonzero throughout the mini-magnetosphere. Thus the nonideal MHD regions in the MPD simulations (Figure 11) are comparable in size to those in the particle simulations, but the region of ion demagnetization is significantly smaller in the MPD simulations.

5. Conclusion

[74] 2.5D particle simulations confirm the earlier MHD result that magnetic anomalies on the surface of the Moon can hold off the solar wind and cause a mini-magnetosphere to form. The solar wind is slowed and heated as it encounters the mini-magnetosphere. Particle acceleration also occurs, but in the mini-magnetosphere, two separate acceleration regions form, one at the subsolar point, primarily for electrons and the second in the downstream region, primarily for ions. The small size of mini-magnetospheres results in a merging of the internal boundaries. A clear difference between the bow shock and magnetopause is not present as it is in large scale magnetospheres.

[75] Decreasing the bulk speed of the solar wind decreases the ion gyroradius, and translates to an increase in the magnitude of the magnetic field on the Lunar surface. This leads to inflation of the mini-magnetosphere. The converse happened when the solar wind bulk speed was increased. Varying the ion to electron mass ratio for the surface ionosphere, on the other hand, had little effect on the size and shape of the mini-magnetosphere.

[76] Small-scale and nonideal MHD effects were included in the fluid simulations, through a modified Ohm's Law. The extra terms also include previously neglected currents and electric fields in the simulations plane. The mini-magnetospheres that formed in the MPD model are nearly identical in size and shape to those in the ideal MHD simulations. Magnetopause currents similar to those seen in the particle simulations are present but are not most prominent in the exact same place, due to differences in the extent of charge separation of the surface ions. Separate bow shock and magnetopause current system do not form in the MPD simulations when the IMF is nonzero, further indicating a merging of the internal boundaries has occurred.

[77] The MPD simulations predict charge separation at the shock surface and near the surface, directly above the anomaly. The charge separation at the shock surface is due to the larger momentum of the ions and results in and electric field and surface plasma currents. The charge separation and nonzero Hall field near the surface are due to nonideal MHD fluid behavior, implying a deficit of ions relative to the electron density near the surface because the ions have become demagnetized. Thus the magnetoplasma dynamics model (MPD) can predict the density distributions of the solar wind and the Lunar electrons, as well as the configuration of the magnetic field. And the behavior of the demagnetized Lunar ions can be inferred from the resulting electric fields and currents.

[78] The next step will be to extend the fluid simulations to 3D. Not only will this allow for fluid transport around all surfaces of the obstacle, but a more realistic model of the magnetic anomalies can be incorporated. And multiple magnetic anomalies over the entire surface can be modeled. Also 3D simulations can investigate if mini-magnetospheres have as dynamic a response to variations in B_y as they do to variations in B_z.

[79] **Acknowledgments.** This work was funded by NASA Graduate Student Research Fellowship NGT5-50285, NSF grant ATM 0105032 and NASA grants NAG5-8089 and NAG5-10962.

References

Dyal, P., et al., Magnetism and the interior of the Moon, *Rev. Geophys.*, *12*, 568–591, 1974.

Harnett, E., and R. Winglee, Two dimensional MHD simulations of the solar wind interaction with magnetic field anomalies on the surface of the Moon, *J. Geophys. Res.*, *105*, 24,997–25,007, 2000.

Hodges, R. R., The lunar atmosphere, *Icarus*, *21*, 415–426, 1974.

Hood, L. L., and C. R. Williams, The lunar swirls: Distribution and possible origins, *Proc. Lunar Planet. Sci. Conf., 19th*, 99–113, 1989.

Hood, L. L., et al., Contour maps of lunar remnant magnetic fields, *J. Geophys. Res.*, *86*, 1055–1069, 1981.

Johnson, F. S., Lunar atmosphere, *Rev. Geophys. Space Sci.*, *9*(3), 813–823, 1971.

Lin, R. P., et al., Lunar surface magnetic field concentrations antipodal to young large impact basins, *Icarus*, *74*, 529–541, 1988.

Lin, R. P., et al., Lunar surface magnetic fields and their interaction with the solar wind: Results from lunar prospector, *Science*, *281*, 1480–1484, 1998.

Parks, G., *Physics of Space Plasmas*, Addison-Wesley-Longman, Reading, Mass., 1991.

Russell, C. T., and B. R. Lichtenstein, On the source of lunar limb compression, *J. Geophys. Res.*, *80*, 4700–4711, 1975.

Sharp, L. R., et al., Orbital mapping of the lunar magnetic field, *Moon*, *7*, 322–341, 1973.

Sonnet, C. P., Solar wind induction and lunar conductivity, *Phys. Earth Planet. Inter.*, *10*(3), 313–322, 1975.

Winglee, R. M., Non-MHD influences on the magnetospheric current system, *J. Geophys. Res.*, *99*, 13,437–13,454, 1994.

Winglee, R. M., and P. J. Kellogg, Electron beam injection, 1, Electromagnetic wave emissions, *J. Geophys. Res.*, *95*, 6167–6190, 1990.

E. M. Harnett and R. M. Winglee, Department of Earth and Space Sciences, University of Washington, Box 351310, Seattle, WA 98195-1310, USA, (eharnett@ess.washington.edu; winglee@ess.washington.edu)